Dynamic observations of vesiculation reveal the role of silicate crystals in bubble nucleation and growth in andesitic magmas

P. Pleše [a,*], M.D. Higgins [a], L. Mancini [b], G. Lanzafame [b], F. Brun [c], J.L. Fife [d,1], J. Casselman [e], D.R. Baker [e]

[a] Département des sciences appliquées, Université du Québec à Chicoutimi (UQAC), 555, boulevard de l'Université, G7H 2B1 Chicoutimi, Québec, Canada
[b] Elettra – Sincrotrone Trieste, S.C.p.A. S.S. 14 km 163.5 in Area Science Park, 34149 Basovizza, Trieste, Italy
[c] National Institute for Nuclear Physics (INFN), Padriciano 99, 34149 Trieste, Italy
[d] Swiss Light Source, Paul Scherrer Institut, 5232 Villigen PSI, Switzerland
[e] Department of Earth and Planetary Sciences (EPS), McGill University, 3450 University Street, H3A 0E8 Montreal, Québec, Canada

ARTICLE INFO

Accepted 19 November 2017

Keywords:
Heterogeneous bubble nucleation
Volcanic degassing
4D *in situ* tomography
3D tomography
Silicate crystals

ABSTRACT

Bubble nucleation and growth control the explosivity of volcanic eruptions, and the kinetics of these processes are generally determined from examinations of natural samples and quenched experimental run products. These samples, however, only provide a view of the final state, from which the initial conditions of a time-evolving magmatic system are then inferred. The interpretations that follow are inexact due to the inability of determining the exact conditions of nucleation and the potential detachment of bubbles from their nucleation sites, an uncertainty that can obscure their nucleation location – either homogeneously within the melt or heterogeneously at the interface between crystals and melts. We present results of a series of dynamic, real-time 4D X-ray tomographic microscopy experiments where we observed the development of bubbles in crystal bearing silicate magmas. Experimentally synthesized andesitic glasses with 0.25–0.5 wt% H_2O and seed silicate crystals were heated at 1 atm to induce bubble nucleation and track bubble growth and movement. In contrast to previous studies on natural and experimentally produced samples, we found that bubbles readily nucleated on plagioclase and clinopyroxene crystals, that their contact angle changes during growth and that they can grow to sizes many times that of the silicate on whose surface they originated. The rapid heterogeneous nucleation of bubbles at low degrees of supersaturation in the presence of silicate crystals demonstrates that silicates can affect when vesiculation ensues, influencing subsequent permeability development and effusive *vs.* explosive transition in volcanic eruptions.

1. Introduction

Volcanic eruptions are commonly driven by the nucleation, expansion (growth) and migration of volatile bubbles (predominantly H_2O and CO_2) following supersaturation of the melt caused by decompression, heating or crystallization (Sparks, 1978). If bubbles nucleate and grow (Fig. 1) at near-equilibrium conditions at low supersaturations, quiescent eruptions are probable, whereas if a significant barrier to bubble nucleation and growth is present a much larger degree of volatile supersaturation is required before nucleation and growth of bubbles, leading to violent eruptions. Understanding bubble growth is a longstanding scientific focus (Gardner et al., 1996; Giachetti et al., 2010; Proussevitch and Sahagian, 2005; Sparks, 1978). The "when" of bubble nucleation in silicate melts has also been extensively studied, but "where" nucleation begins has not received equal attention (the reader is referred to the review by Fiege and Cichy, 2015).

The conditions of bubble nucleation, either homogeneously within the melt, or heterogeneously on a pre-existing melt-crystal interface (Fig. 1), remain obscure. Due to large density differences between a gas bubble and its surrounding magma (melt + crystals), bubbles can be an easily displaced phase. Their mobility can potentially lead to erroneous assumptions of the bubbles' initial position, based upon observations of the bubbles' final positions in post-process (*ex situ*) samples. Most previous studies of bubble nucleation and growth investigated natural volcanic samples and quenched experimental run products that only provide the final state, from which the initial conditions of a time-evolving magmatic system must then be inferred. Knowledge of all aspects of nucleation and growth of bubbles in magmatic systems is one of the keys to a better understanding of volcanic eruption mechanisms.

The nucleation location is influenced by the interfacial energy between the exsolved fluid and molten or solid phases (Hurwitz and Navon, 1994). In a heterogeneous bubble nucleation scenario a melt-crystal interface already exists prior to bubble nucleation, hence

* Corresponding author at: 555, boulevard de l'Université, Chicoutimi, Quebec G7H 2B1, Canada.
E-mail address: pia.plese1@uqac.ca (P. Pleše).
[1] Previously with.

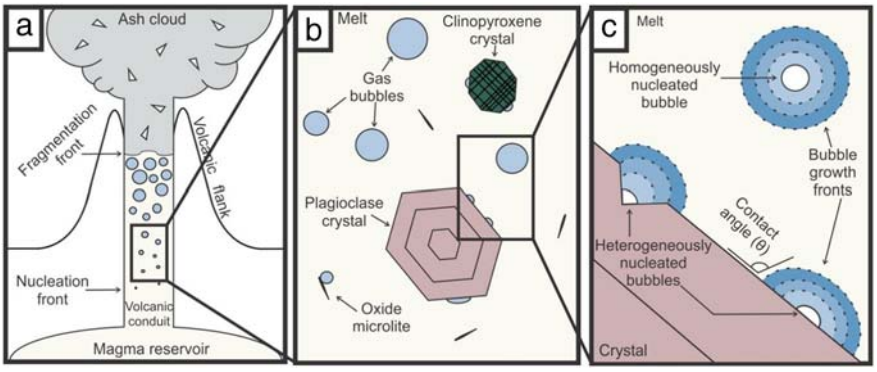

Fig. 1. Model of bubble formation in silicate melts. a) The nucleation front is marked by the first appearance of bubbles. The fragmentation front marks the transition from a bubbly melt to a gassy spray (Gardner et al., 1996; Proussevitch and Sahagian, 2005; Sparks, 1978). The ash cloud contains particles originating from the volcanic conduit. b) The magma within a conduit can contain crystals of various sizes and compositions. c) Depending on pressure, temperature, and melt composition, bubbles can nucleate homogeneously or heterogeneously. The contact, or wetting, angle (θ) is the angle between the bubble and the crystal measured in the melt (Fiege and Cichy, 2015; Gualda and Ghiorso, 2007).

the energy needed to nucleate a bubble is decreased compared to homogeneous bubble nucleation, making the heterogeneous case more favourable and possible at lower volatile supersaturations (Hurwitz and Navon, 1994; Landau and Lifshitz, 1980; Navon and Lyakhovsky, 1998). Once a melt becomes supersaturated in a volatile component, the pairing of a bubble and a crystal is always a thermodynamically favoured starting point, achieved either by heterogeneous bubble nucleation or by attachment of existing bubbles to crystals (Gualda and Ghiorso, 2007).

Due to the interfacial energies involved (bubble-crystal, bubble-melt and melt-crystal), the wettability of a crystal by a bubble (where wetting is the ability of the volatile phase to remain in contact with the solid phase; Young, 1805) is considered a representation of the efficiency of a crystal to nucleate a bubble (Hurwitz and Navon, 1994). When comparing different bubble-crystal pairs, various crystal efficiencies at nucleating bubbles are inferred from the values of the contact angle θ between them (Fig. 1) and the critical value is set to be 68° (Hurwitz and Navon, 1994). Above this value, the crystal is considered efficient at nucleating bubbles, and below this value, the crystal is considered inefficient (Hurwitz and Navon, 1994). Oxides are currently considered favourable bubble nucleation sites (*e.g.* Gualda and Anderson, 2007; Gualda and Ghiorso, 2007) due to their significant compositional and bonding differences from the encompassing silicate melt (Mysen and Richet, 2005) as well as because of their poor wettability by the melt (Adamson and Gast, 1997).

Most experiments on heterogeneous bubble nucleation (*e.g.* Gardner et al., 2000; and references in Fig. 2) were conducted using rhyolitic melts where bubbles were mostly found on oxide microlites such as titanomagnetite, with very few reported on silicates. However, due to instrumental limitations, bubble-oxide contact angles were rarely measured and not universally found to be greater than 68° (Fig. 2). The data for bubble-silicate crystal contact angles is equally sparse, since silicate crystals are generally excluded from degassing studies (the starting melt is commonly without crystals), but where measured, θ was smaller than seen for oxides (except for biotite; Hurwitz and Navon, 1994). We must stress that all the contact angles reported so far in the literature were measured in 2D, and the plane in question did not necessarily pass through the bubble's maximum cross-section.

Recently, additional mechanisms of inducing homogeneous bubble nucleation have been hypothesized, such as the passage of seismic

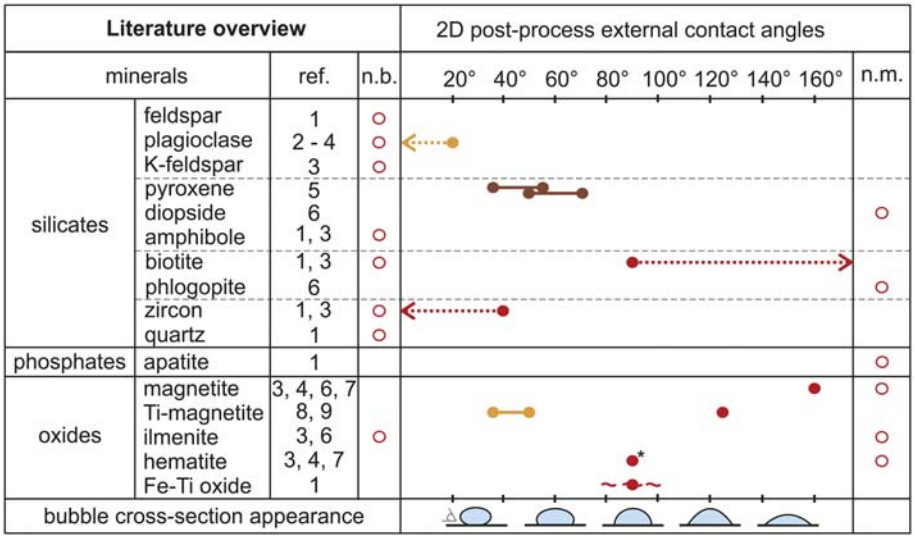

Fig. 2. Literature compilation of reported bubble-crystal 2D post-process external contact angles. Mineral names are those used in the study. References: 1 = Hurwitz and Navon (1994), 2 = Eichelberger and Hayes (1982), 3 = Cluzel et al. (2008), 4 = Gardner (2007), 5 = Larsen (2008), 6 = Navon and Lyakhovsky (1998), 7 = Gardner and Denis (2004), 8 = Mangan and Sisson (2005), 9 = Mangan et al. (2004). Abbreviations: n.b. = no bubbles present on the crystal surface, n.m. = no measurement of contact angles is reported even though bubbles are present on the crystal surface. Yellow colour represents dacite, red rhyolite and brown K-phonolite. The star sign indicates a calculated, not measured, value. The wavy broken line represents a value around 90°, and dotted arrows represent values reported as lesser or larger than a certain value. The number of measurements was not indicated in any of the studies. (For interpretation of the references to colour in this figure legend, the reader is referred to the web version of this article.)

waves through a melt (Acocella, 2014; Manga and Brodsky, 2006). If homogeneous nucleation can be achieved more easily than previously thought, and heterogeneous nucleation is always easier to achieve than homogeneous, could silicate crystal's surfaces play a role in bubble nucleation? The specific goals of this study were to explore bubble nucleation efficiencies of some silicate crystals based on the following observations:

1) Even though they are seen as inefficient, silicate minerals with attached bubbles have been reported, sometimes even with the same 2D contact angle θ value as measured on oxides (Fig. 2);
2) The mineral abundance conundrum – iron oxides, not a dominant crystal phase in silicate melts, are considered the most efficient crystals for heterogeneous bubble production (Hurwitz and Navon, 1994). However it has been questioned whether oxides alone can provide enough nucleation sites to account for the bubble number densities recorded (Mangan and Sisson, 2000; Mourtada-Bonnefoi and Laporte, 2004). If, within the investigated samples, oxide crystals are not found in direct contact with bubbles, then homogeneous nucleation is deemed dominant (*e.g.* Gualda and Ghiorso, 2007) because any silicate crystals that might be present within the sample are not taken into consideration.
3) Bubbles are not stationary in silicate melts and can detach from, or attach to, crystals (Gualda and Ghiorso, 2007), but this process has never been directly observed and hence generally not taken into account, although several authors have considered this possibility (Belien et al., 2010; Blythe et al., 2015; Gualda and Ghiorso, 2007; Mangan and Sisson, 2000).
4) The contact angle θ does not necessarily remain constant throughout a bubble's growth (Gardner and Denis, 2004), so it is difficult to determine from observations of post-process samples the instant when the bubble was "frozen" (by natural solidification or experimental quench). Therefore, we do not know if the sample approached kinetic equilibrium and if the measured contact angle is the final one.

In order to examine the first seconds of bubble formation, we employed 4D X-ray tomographic microscopy as a tool to image and record nucleation and growth, therefore building on the pioneering work on *in situ* 2D observations of bubble nucleation and growth (Bagdassarov et al., 1996; Gondé et al., 2006, 2011; Applegarth et al., 2013; Masotta et al., 2014) with the latest developments in 3D and 4D imaging of geological materials (Bai et al., 2008; Baker et al., 2012a, 2012b; Pistone et al., 2015a, 2015b).

2. Materials and methods

2.1. Hydrous glass synthesis

The starting materials for the vesiculation experiments were synthesized using a piston-cylinder apparatus at McGill University (Montreal, Québec, Canada). Rock powder of andesitic composition (AT-29 with 56.8 wt% SiO_2, from Baker and Eggler, 1987) was added to Pt-capsules, along with silicate crystals and 0.25–0.5 wt% H_2O. An andesitic melt composition was chosen to contrast with existing rhyolitic and dacitic data and because it corresponds to compositions of arc-type volcanoes, which are frequently explosive (Sakuyama and Kushiro, 1979; Sigurdsson et al., 2015). The silicate crystals were plagioclase (gem-quality labradorite) and clinopyroxene (augite, from Baker and Eggler, 1987), and both were crushed before being added to the capsule. They were chosen to represent common magma phenocrysts and thus introduce crystal surfaces of minerals thought to be compositionally too similar to the melt to be efficient at nucleating bubbles (Mangan et al., 2004). These minerals contain low concentrations of inclusions (some oxides in the clinopyroxene) and they are nominally anhydrous. The added amount of water was kept low to create melts that would be only slightly supersaturated at 1 atm during the dynamic tomography experiments. The capsules were welded shut and checked for water loss by weighing before and after an hour of heating in a 110 °C furnace.

Three synthesis experiments were performed at 1275 °C, 1 GPa to create crystal-bearing hydrous glasses. The durations of the experiments were chosen to be sufficient for water to homogenize by diffusion in the capsule, but short enough so that the added crystals did not dissolve. The added crystals represented 30 vol% of each capsule in each run (before heating and pressurization). The first run had two capsules, one with AT-29 + clinopyroxene seed crystals ("1a") and the other with AT-29 + plagioclase ("1b"), both with 0.5 wt% H_2O and held at pressure and temperature conditions for 1 h before isobaric quench. The second run also had two capsules, both with AT-29 + clinopyroxene crystals, but with one containing 0.5 wt% H_2O ("2a") and the other 0.25 wt% H_2O ("2b"), both performed for 20 min. The third run was also of 20 min duration and had only one capsule ("3"), containing both AT-29 + clinopyroxene + plagioclase crystals and 0.5 wt% H_2O. The H_2O values reported here represent the amounts added to the starting material, not the amounts in the final glasses. The quenched glass + crystal run products were removed from their Pt-capsules, which resulted into their fragmentation into several pieces.

2.2. X-ray computed tomography (CT)

X-ray tomographic microscopy (microCT) was used to characterize the synthesis and vesiculation experiments in this study. This technique provides 3D images of specimens and is well-established in the geoscience community (Baker et al., 2012a, 2012b). In order to fully characterize both the starting materials and the run products of the 4D vesiculation experiments, different X-ray tomography instruments were used. A short overview of the tomography methods applied, the main differences between them, and questions aimed to be answered by them can be found in Table 1.

2.3. Conventional X-ray microtomography (microCT)

Pieces of glass + crystals from several synthesis samples were imaged with a Skyscan 1172 desktop X-ray tomography machine at the MIAM laboratory of McGill University to ascertain if bubbles had formed, and if the silicate crystals had melted, during the synthesis. The scanning conditions were 55 kV, 179 μA, Al filter, camera binning 2 × 2, source-to-sample distance = 38.68 mm, camera-to-source distance = 345.101 mm, camera pixel size = 11.56 μm, image pixel size = 2.59 μm, exposure time = 0.2065 s, rotation step = 0.4°, projection number = 902 over 360°, frame averaging = 3, random movement = 10.

A sample from Stromboli volcano was also scanned so that our experimental results could be compared to a natural material. The scanning conditions were 44 kV, 226 μA, Al filter, camera binning 4 × 4, source-to-sample distance = 36.1 mm, camera-to-source distance = 345.101 mm, camera pixel size = 11.56 μm, image pixel size = 4.84 μm, exposure time = 0.474 s, rotation step = 0.68°, projection number = 531 over 360°, frame averaging = 4, random movement = 10.

2.4. Conventional X-ray nanotomography (nanoCT)

NanoCT was used to obtain 3D scans of specific regions of interest within the glass + crystals starting materials, with the goal of investigating the possible presence of cracks at the crystal-glass interface and for locating plagioclase in the samples; this was important since both of these features were not clearly visible with the microCT. The 3D scans were performed on the Zeiss Xradia 520 Versa at the Cell Imaging and Analysis Network of McGill University. The scanning conditions were 70 kV, 85 μA, no filter, camera binning 2 × 2, source-to-sample distance = 10.23 mm, camera-to-source distance = 30.24 mm, optical magnification = 40×, image pixel size = 0.22 μm, exposure time =

Table 1
Summary of different tomography methods used and questions to be answered with them. Conventional refers to stand alone XRT instruments, microCT = micro-scale computed tomography, nanoCT = nano-scale computed tomography, SR = synchrotron radiation. Pixel size refers to 2D image elements. Phase contrast is a technique applied during imaging, and phase retrieval is a set of algorithms applied while reconstructing the imaged radiographs.

Tomography method	Radiation type	Pixel size	Phase contrast	Phase retrieval	Question asked
MicroCT	Conventional, *ex situ*	2.59 μm	No	No	1) Did bubbles form? 2) Did clinopyroxene crystals melt during synthesis experiments?
NanoCT	Conventional, *ex situ*	0.22 μm	Yes	No	1) Did plagioclase crystals melt during synthesis experiments? 2) Did cracks form at the crystal-glass interface?
4D SR microCT	Synchrotron, *in situ*	3 μm	Yes	Yes	When do bubbles form and how rapidly?
SR microCT	Synchrotron, *ex situ*	0.65 μm	Yes	Yes	Where did bubbles form?

25 s, rotation step = 0.4°, projection number = 935 over 360°. The microCT and nanoCT analyses described above were performed with the aim of learning as much as possible about the synthesized samples without destroying them.

2.5. 4D in situ synchrotron X-ray tomographic microscopy

Ambient pressure 4D vesiculation experiments were performed at the TOmographic Microscopy and Coherent rAdiology experiments (TOMCAT) beamline of the Swiss Light Source at the Paul Scherrer Institut in Villigen, Switzerland (Stampanoni et al., 2006). Approximately 0.5–1 mm^3-sized pieces of the synthesized andesitic hydrous glasses + crystals were mounted in a cylindrical, ceramic sample holder and heated using the laser-based heating system at TOMCAT (similar to earlier systems described in Fife et al., 2012). The system incorporates two 150 W, class IV diode lasers operating at 980 nm and projecting oval laser spots (4 mm wide by 6 mm high). The temperatures were measured with a pyrometer (Fife et al., 2012) that was calibrated using the temperature of the first appearance of bubbles in the sample as measured by a type K thermocouple in a laboratory furnace at McGill. The temperatures are accurate to with ±20 °C. A thermal gradient is always present in the laser furnace and we tried to minimize its effect by always placing our sample at the center hot spot of the furnace. Due to the lack of sufficiently sensitive thermal sensors we could not quantify the thermal gradient present.

Three pieces from each of the five charges were heated and imaged separately at TOMCAT; this provided an opportunity to confirm the consistency of events occurring during a single heating sequence with others originating from the same charge. The initial heating regime was 2 °C/s until a chosen temperature above the glass transition temperature was reached. The sample was held at constant temperature until the end of the experiment and then quenched by turning off the laser system. The goal of rapid heating at 1 bar was to simulate isothermal decompression from the saturation pressure of the sample (dependant on its water content).

Imaging was performed using the GigaFRoST detector (Mokso et al., 2017) connected to an optical microscope and incorporating a continuously adjustable magnification tuned to approximately 4×. Polychromatic radiation was filtered to 5% power, and the sample-to-detector distance was set at 280 mm, optimized for phase-contrast imaging of these materials. Each 3D tomographic scan is based upon 501 projections acquired over 180° in 0.5 s with a 3 μm pixel size. Real-time radiographs (*i.e.* the 2D projection images acquired by the camera prior to the tomographic reconstruction) of one piece of each sample were examined to determine the approximate temperature when bubbles first appeared (as in Bai et al., 2008). Subsequent scanning began at a temperature slightly below this temperature in order to capture bubble nucleation. All samples were scanned *continuously* for 50 s, and 100 3D datasets (from here on called timesteps, from t_1 at 0.5 s to t_{100} at 50 s) were produced for each sample. Tomographic reconstructions were obtained after the application of a phase-retrieval algorithm (modified from Paganin et al., 2002), to the acquired projections, with the following parameters: X-ray energy = 30 keV, $\delta = 5.1 \times 10^{-7}$ and $\beta = 5.1 \times 10^{-9}$ (δ and β are dimensionless real numbers whose ratio is one of the input parameters for phase-retrieval – for more information see Paganin et al., 2002).

2.6. High resolution ex situ synchrotron X-ray tomographic microscopy

To examine more closely some especially interesting features that developed during the *in situ* scanning, selected experiments were re-imaged after their conclusion using high-resolution, monochromatic X-rays and phase-contrast imaging on the TOMCAT beamline. This was critical for determining the post-process position of bubbles with regard to crystal surfaces, and cross-referencing the phase contrast scan position of each individual bubble with the *in situ* measurement. The imaging of crystals and bubbles within a silicate matrix by conventional absorption X-ray tomographic microscopy is limited by the contrast in their X-ray absorption. This is especially troublesome for plagioclase crystals, which can be practically indistinguishable from the melt. This lack of phase contrast between plagioclase and glass can prove potentially misleading when bubble nucleation is investigated because it is difficult to determine if the bubble is on the crystal surface. To overcome this issue, propagation-based phase contrast imaging was also utilized for these *ex situ* scans; this method uses the phase information of a material to enhance image contrast (Polacci et al., 2006). An energy of 27 keV was used and a standard optical microscope with 10× magnification was connected to the pco.Edge 4.2 (PCO, Germany) camera, resulting in a 0.65 μm pixel size. The sample-to-detector distance was decreased to 80 mm, and 1501 projections were acquired over 180° of continuous rotation, resulting in a single 3D scan acquired in approximately 20 min. A full dataset was reconstructed several times, first without and subsequently with phase retrieval. In the latter case, the δ and β parameters were varied in order to optimize the δ/β ratio by selecting the minimum value for which the fine microstructures were visualized and the phase contrast 'artefacts' were reduced in the resulting slices. The final selected parameters were: $\delta = 5.1 \times 10^{-7}$ and $\beta = 3.5 \times 10^{-9}$.

2.7. Volume segmentation

In order to determine the total volume of bubbles generated, the entire sample volume was tracked as it inflated during heating. The initial volume was taken as the one at timestep t_1, and the sample was segmented by grouping both sample and crystal voxels together and binarizing them (values 90–255 on 8-bit volumes), using Fiji (Schindelin et al., 2012) and Pore3D (Brun et al., 2010). If a crack was present within the sample at t_1, it was not attributed to the sample. The final sample volume was the one at timestep t_{100} and the sample (glass + crystals) was binarized again (same values). For some samples, the entire sample volume at t_{100} could not be successfully segmented automatically, due to very thin bubble melt/glass films comprising the outer sample outline. In such cases, manual segmentation was used to assign these voxels to the melt, while making certain that the film thickness is preserved. All the segmented volumes were calculated using Pore3D and the difference between the volume at t_{100} and at t_1 was the total bubble volume.

Several bubble-crystal aggregates were chosen for 3D visualization to illustrate bubble-crystal relations. A sample sub-volume that contained the objects of interest was chosen and its voxels were segmented as bubbles and crystals (thresholding values 0–140 for bubbles and 200–255 for clinopyroxene, on 8-bit volumes), and the segmentation was always finished manually. Certain regions of the subvolume were excluded from segmentation to ease the visualization, such as bubbles that nucleated on neighbouring crystals. The segmentation was done by semi-automatic thresholding in 3D for clinopyroxene and bubbles and manually for plagioclase, *i.e.* simultaneously on 3 sets of 2D slices corresponding to 3 slice orientations (XY, XZ and YZ), using Avizo Fire® (Visualization Sciences Group). The extent of surface smoothing was restricted so that the thin layer of bubbles on the crystal remains visible. Voxels corresponding to melt/glass films between bubbles were assigned to the bubble phase to facilitate 3D visualization. The number of bubbles on individual crystals was determined by applying the watershed algorithm (MorphoLibJ plugin of ImageJ) on the post-process samples imaged at submicron resolution on TOMCAT (Table 1), where the resolution and border contrast enhanced their visibility. However, even in this case the melt films proved difficult to segment, either automatically or manually, so the number of bubbles obtained represents a minimum value.

2.8. Contact angle measurements in 3D

The 3D contact angle between a bubble and a crystal (Fig. 3) was defined as the angle whose vertex touches the bubble-crystal-melt contact line, one arm is tangential to the bubble surface (plane YZ) and the other lies on the crystal surface (plane XY); this angle lies in the same plane as the central axis of the bubble (Fig. 3) which is defined by the bubble's maximum height. When identified, the 2D slice was then rotated around this axis in order to measure the contact angle at six different places (3 paired values) on the bubble-crystal-melt contact line. The measurements were done using the Avizo® software within the volume rendering, using the "slice" and "angle measurement" tools. The software allows rotating any selected slice around a user specified axis or direction. Measuring the contact angle through such identification of a specific 2D slice within a 3D volume, is a novel approach that provides improved results over measuring the contact angle on an arbitrary 2D slice. These measurements were repeated for different timesteps of the experiment to track the change in the contact angle for a specific bubble. Only bubbles that were hemispherical caps and had angles on each side differing by less than 5° for all timesteps were used for contact angle measurements.

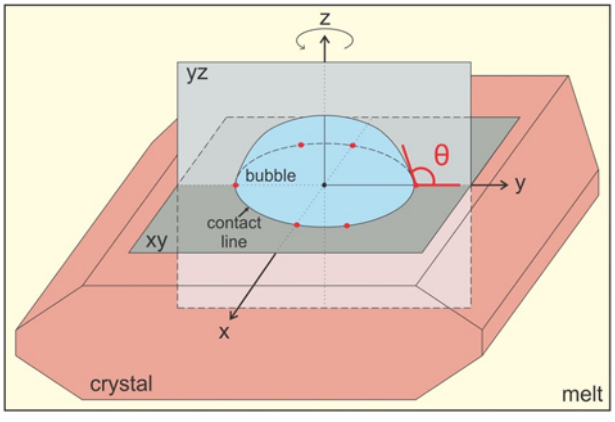

Fig. 3. Schematic model of the 3D bubble-crystal contact angle measurement. Once planes XY and YZ have been located (in which the two arms of the angle lie) within the 3D volume, the YZ plane was rotated around the Z axis so the contact angle can be measured multiple times along the contact line (measurement location represented by red dots). Each contact angle measurement in a chosen YZ plane was performed twice, on each side of the bubble. (For interpretation of the references to colour in this figure legend, the reader is referred to the web version of this article.)

2.8.1. Scanning electron microscopy

To compliment the 3D and 4D data with a well-recognized 2D analysis, and to compare the results, one post-process sample was examined with a Hitachi SU-3500 Variable Pressure-SEM using a BSE detector. One sample was ground down to a target slice identified from the sample's 3D reconstruction. The amount of grinding and polishing was constrained by the fragile nature of the foamy post-process samples. The accelerating potential was 30 kV and the beam current was 0.102 mA.

2.9. X-ray tomographic microscopy at APS

The experimental samples produced were also visually compared to a natural Montserrat sample, scanned at the GeoSoilEnviroCARS beamline, of the Advanced Photon Source synchrotron (Illinois, U.S.A.). The X-ray beam had an energy of 25 keV, the camera magnification was 10× and the image pixel size was 1.24 μm.

3. Results

3.1. Starting glass + crystals

Pieces of each of the starting materials for the vesiculation experiments were examined with conventional microCT. The scans showed that no bubbles were present. The large clinopyroxene crystals were clearly visible in all relevant samples, as were oxide crystals that grew during synthesis experiments. Plagioclase crystals were not detected with conventional microCT, so a nanoCT scanner was used to check for their presence. The nanoCT scans were too noisy for quantification, but plagioclase crystals were nonetheless successfully detected, as well as cracks within the samples (Fig. 4). These cracks were most likely formed during isobaric quench at the end of the synthesis, or during the samples' removal from the Pt-capsule. The cracks are not systematically oriented along any crystal boundary, but instead cut through the sample and crystals equally, occasionally following part of the crystal surface.

3.2. In situ vesiculation

The determination of the temperature at which bubbles first appeared was performed at TOMCAT in the same manner as the 1 atm furnace at McGill. One piece from each charge was heated and observed only through radiographs (2D projection images). The correction factors obtained are presented in Table 2 and henceforth all temperatures discussed are the corrected values. Previous work demonstrated that bubble nucleation begins above the glass transition temperature (Bagdassarov et al., 1996), which for glasses of similar composition and water concentration was determined to be 467 °C ± 2.5 °C (Giordano et al., 2005).

Thermal gradients within experimental charges are always present, but we have made every effort to minimize this effect by positioning the sample close to the laser hotspot. A thermal gradient is nonetheless present, as seen through a delay in bubble nucleation at different heights within the sample. The lowermost part of the sample nucleated bubbles later than the middle and upper parts; hence it is considered cooler in temperature.

Heterogeneous nucleation always occurs first on the silicate crystals in the furnace hotspot, and in other portions of the sample further away from the hotspot shortly thereafter. There is a 20 second lag time between heterogeneous bubble nucleation on silicate surfaces closer and further away from the hotspot. Heterogeneous nucleation on oxide surfaces or homogeneous nucleation within the melt (in any part of the sample), never occurred before heterogeneous nucleation on silicate surfaces in the coolest part of the sample. Hence, we conclude that the same processes of bubble nucleation were at work throughout

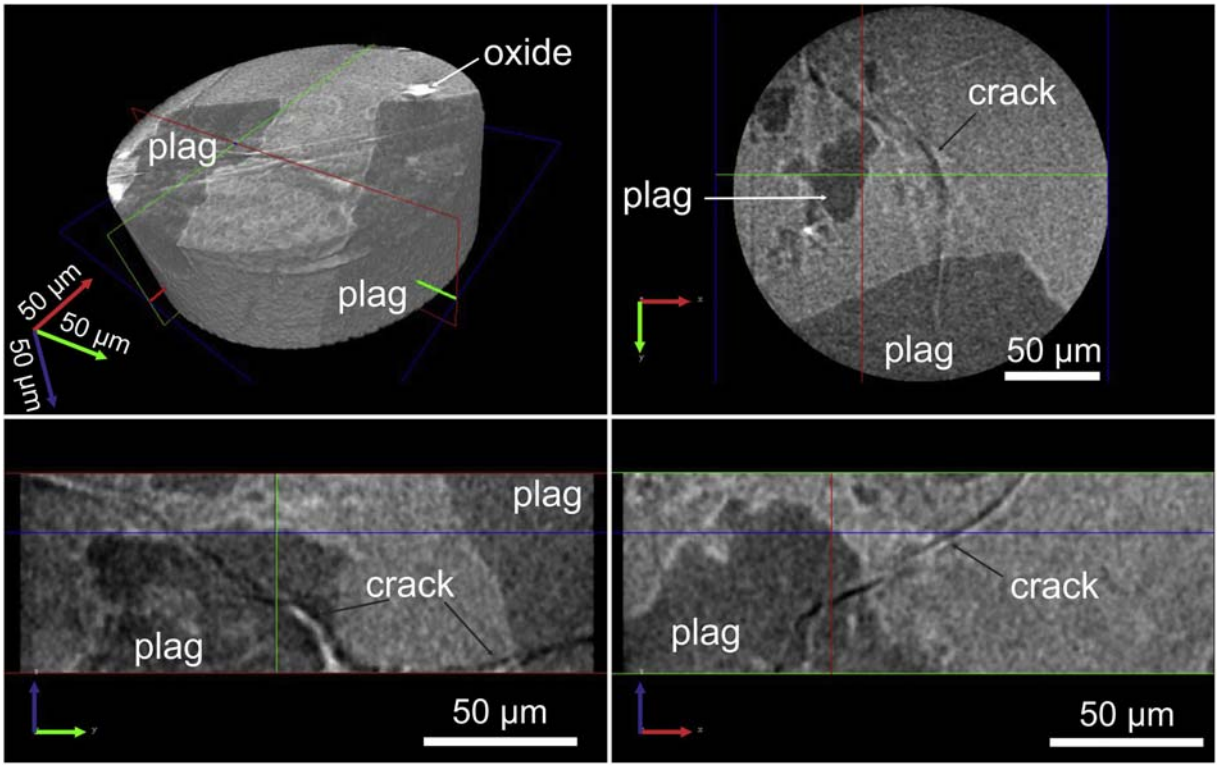

Fig. 4. 3D visualization and three orthogonal 2D slices of an *ex situ* nanoCT scan of a region of interest within a starting material sample. Plag = plagioclase. In the 3D visualization, the length of each axis of the 3D scale represents 50 µm in its respective direction. Plagioclase crystals, oxide crystals and cracks are clearly visible. The position of the cracks does not follow the plagioclase crystal borders.

the entire sample volume. That is to say, the nucleation events occurred in the same order throughout the sample, but there was a time delay between the "hotter" and the "cooler" part of the sample. Thus, if a clinopyroxene in the "hotter" part of the sample nucleated more bubbles than a plagioclase in the "cooler" part, the clinopyroxene is not more efficient at nucleating bubbles. Hence, to determine the nucleation event timeline we considered only the middle and lower sections of the sample volumes and compared different crystals that were placed at similar heights in the sample, thus comparing nucleation events occurring at similar temperatures.

Four representative samples are presented in detail here, but there are other pieces from the same charges that share their features. A summary of the data obtained can be found in Table 2. From timesteps t_1 to t_{100} samples underwent an increase in volume due to bubble nucleation and growth (Fig. 5). Inspection of 3D volumes for each timestep showed the location, time and temperature of bubble nucleation (Figs. 6 and 7). The total bubble volume produced in the only sample with lower H_2O wt% does not significantly differ from those in samples with higher H_2O wt%.

Large clinopyroxene crystals and oxides were the only crystal phases clearly distinguishable in the *in situ* scans (Fig. 6), as in the case of the microCT. Observations of the sample during heating showed that the first bubble formation was in part clearly associated with clinopyroxene crystals. The topology of such bubbles was clearly hemispherical on the side facing the melt (outward), and planar on the other side (inward), suggesting nucleation on the surface of an object and not within a melt. Bubbles that nucleated away from the clinopyroxene crystals formed hollow sphere-like structures in 3D volumes. Importantly, during these early timesteps, no bubbles nucleated on oxides.

Table 2
Quantitative data for four representative samples. The sample name corresponds to the piston cylinder run (1, 2, 3), the charge within that run if there were several (a, b) and the experiment number at TOMCAT (6, 7, 8, 11). Plag = plagioclase, cpx = clinopyroxene, n.p. = not present, n.o. = not observed, t_1 = start of acquisition, t_{100} = end of acquisition. The event numbers correspond to those on Fig. 5. The temperature error is ±20°.

Sample name	1b-11	2b-8	3-6	3-7
# of plagioclase crystals in sample	35	n.p.	7	7
# of clinopyroxene crystals in sample	n.p.	29	19	30
# of oxide crystals in sample	9	24	218	7
Sample volume at t_1 (mm^3)	0.256	1.045	0.249	0.167
Temperature correction factor	1.25	1.18	1.3	1.3
Temperature at t_1 (°C)	600	620	540	550
Temperature of heterogeneous bubble nucleation on plagioclase (°C) = event 1	660	n.p.	550	570
Temperature of heterogeneous bubble nucleation on clinopyroxene (°C) = event 2	n.p.	650	560	570
Temperature of homogeneous bubble nucleation within the melt = event 3	690	n.o.	600	590
Temperature of heterogeneous bubble nucleation on oxide (°C) = 4	n.o.	650	670	n.o.
Temperature of sample inflation (°C) = event 5	n.o.	650	615	600
Sample volume at t_{100} (mm^3)	0.289	1.151	0.487	0.590
Percentage of sample volume change (%)	13	10	95	253
Total bubble volume at t_{100} (mm^3)	0.033	0.106	0.237	0.423

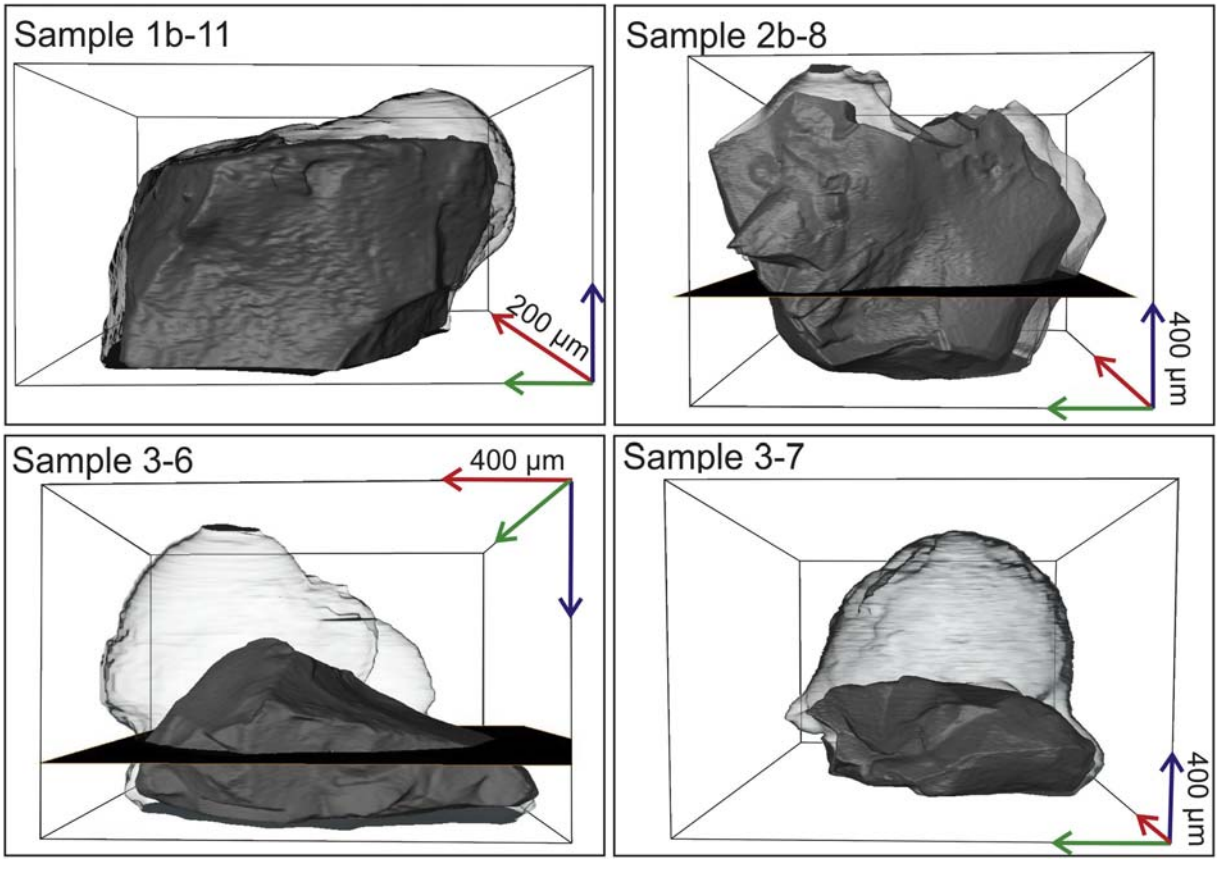

Fig. 5. 3D representation of 4 representative samples of melt + crystals + bubbles. The smaller, dark grey volume is the unvesiculated sample volume at t_1 (start of the experiment) and the larger, light grey volume is the vesiculated sample volume at t_{100} (experiment's end). The black plane passing through samples 2b-8 and 3-6 represents the locations of 2D slices presented in Fig. 7. For each sample all three axes of the 3D scale represent the same length, in their respective directions, which is 200 µm for sample 1b-11 and 400 µm for all other samples.

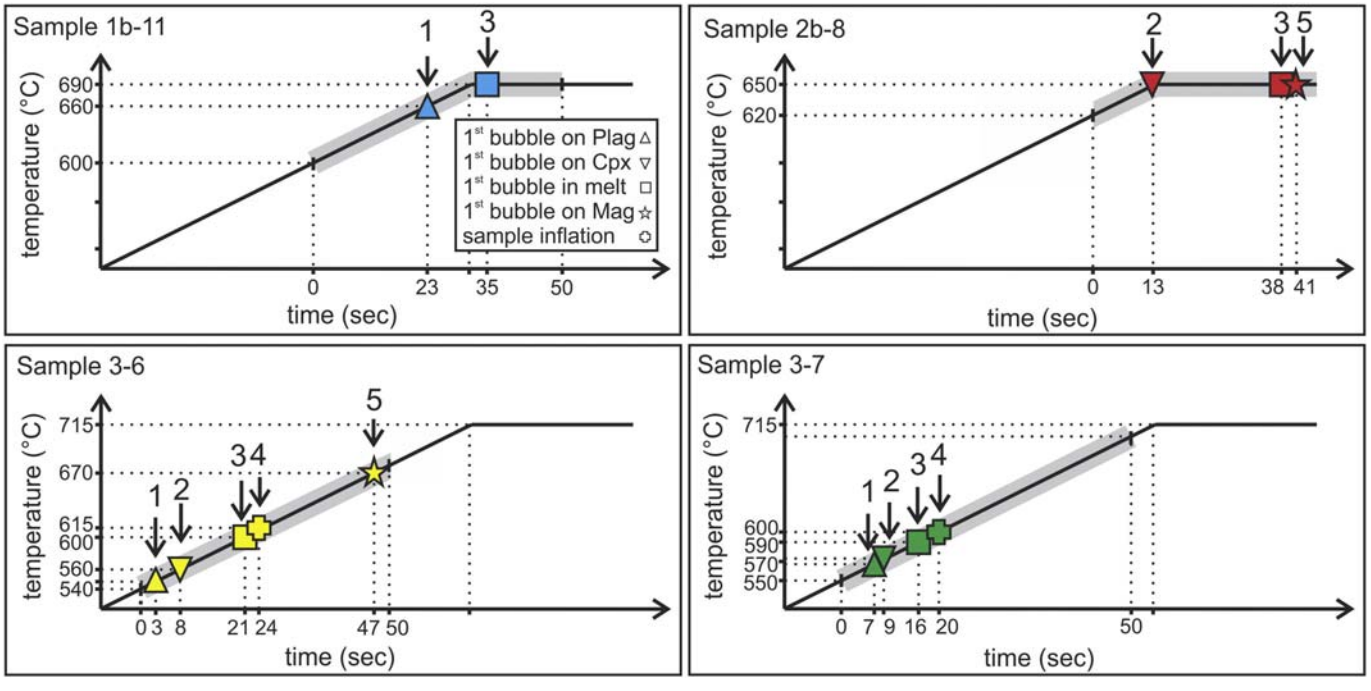

Fig. 6. Timeline of nucleation events during the *in situ* heating experiments. The x-axis shows time, with the starting value of 0 representing when scanning began (t_1), and the final value 50 when it ended (t_{100}). The y-axis shows temperature. The black line represents the heating regime during each experiment, with the part of it enhanced in grey showing when scanning was performed. The symbols represent the T-t point at which specific events occurred. The order of events (1–5) corresponds to the event order in Table 2. Not all samples exhibit all possible events.

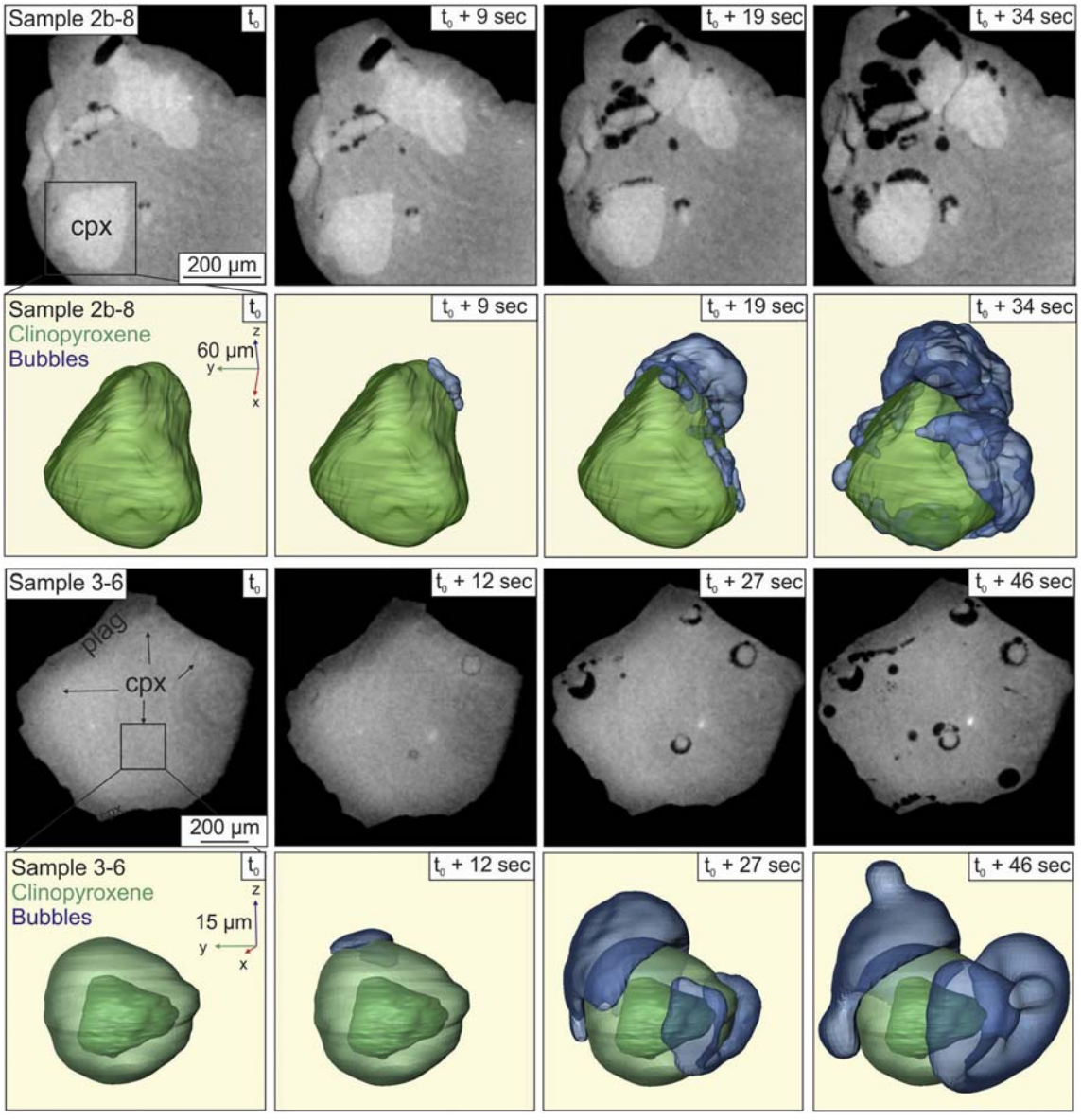

Fig. 7. 2D and 3D sequences of bubble nucleation and growth on silicate crystals during heating. Sample 2b-8 contains only clinopyroxene (cpx) crystals, while sample 3-6 contains both clinopyroxene and plagioclase (plag) crystals. Note that solitary bubbles apparently within the melt in the 2D sequences are located on crystal surfaces below or above the presented slice. The presented 2D slices are located in the lower part of the cpx and in the middle of the plag, respectively. The locations of the 2D slices within the entire samples are shown on Fig. 5. All three axes of the 3D scale represent the same length, in their respective directions. The clinopyroxene in sample 2b-8 maintained its original surfaces, while the one in 3-6 has a core and a rim around it. The core can only be distinguished from the *ex situ* scans from TOMCAT and has been incorporated to the *in situ* 3D visualization. The temperature change for both samples can be seen on Fig.5.

Bubbles initially grew by maintaining their initial topology, until they encountered adjacent bubbles, after which their growth was confined to the hemispherical side. This further confirms that growth on the planar side was impeded by a solid surface. In order to clearly determine whether the other objects around which other bubbles (hollow sphere like ones) nucleated were crystals as well, the *in situ* timesteps were compared with the *ex situ* scans for each sample (Fig. 7). The phase border enhancement revealed the presence of both plagioclase crystals and small clinopyroxene crystals, both of which had bubbles associated with them, *i.e.* nucleating on their surfaces. Combining these two tomographic methods allowed us to accurately determine a bubble's starting position and build a nucleation timeline (Fig. 6).

Larger clinopyroxene grains were easily distinguishable in tomographic volumes, but smaller crystals proved to be more difficult to discern (Fig. 7). Clinopyroxene crystals appeared homogeneous without phase contrast in *in situ* scans but turned out zoned in *ex situ* scans. SEM analysis showed that these clinopyroxenes have a core and rim that are compositionally the same, even though the outer part displays a spike-like radial texture. Since neither plagioclase nor clinopyroxene were in exact equilibrium with their surrounding melt during starting material synthesis, we conclude that the smaller clinopyroxene crystals started to melt, but the partially molten part did not have time to mix with the surrounding melt, producing an inner core and outer rim appearance. The reason we see no difference between the core and the outer rim with *in situ* scans is that it is a structural and not a compositional difference. Large clinopyroxene crystals do not exhibit such spike-like radial textures (Fig. 7).

The clinopyroxene crystals used as seeds are natural augites and they contain inclusions of oxides, which are visible in the scanned volumes. Since the inclusions are randomly distributed within the clinopyroxene, there were also most likely present in the portions of the smaller clinopyroxene crystals that partially melted during starting material synthesis (*i.e.* in the outer rim). The question then arises if they

could have been pushed out to the new outer rim-melt interface, where then they could have acted as bubble nucleation sites during *in situ* vesiculation. We inspected both the *in situ* and the *ex situ* scans for evidence of such oxide placement, and found none. We also inspected the larger non-molten clinopyroxene crystal surfaces and found that if an oxide inclusion/impurity was present at the interface it did not act as a bubble nucleation site, while the impurity-free, non-molten clinopyroxene surfaces did. If the oxides within the clinopyroxene were the underlying reason for what appears as heterogeneous nucleation on clinopyroxene surfaces, we would expect the other oxides present within the melt to behave the same, which they do not. Combining these observations with those of inclusions and plagioclases also nucleating bubbles, we see no evidence that oxide impurities within the clinopyroxene crystals were the reason for heterogeneous bubble nucleation on clinopyroxene surfaces.

Several plagioclase-bubble and clinopyroxene-bubble aggregates were isolated from the phase contrast scan of sample 3-7 and divided into sub-volumes to determine the number of bubbles that nucleated on the respective crystals. Bubbles were segmented by combining the watershed and morphological segmentation algorithms of ImageJ. Due to the proximity of some bubbles (Figs. 7 and 8) the values obtained only represent the minimum numbers of bubbles nucleated, and it was often clear with the naked eye that the protocols applied could not discern all the small bubbles present. For plagioclases the minimum number of bubbles was between 110 and 365, while for clinopyroxenes between 20 and 121. To compare, in sample 2b-8, a single oxide crystal out of the 24 present nucleated 2 bubbles, and in sample 3-6 a single oxide out of the 218 present nucleated 6 bubbles.

There is a striking difference in the number of bubbles that nucleated on silicate crystal surfaces compared to those on oxide surfaces in our experiments (2 and 6 on a single oxide *vs* tens of bubbles on almost all clinopyroxenes, and hundreds on almost all plagioclases), which contrasts with earlier research (*e.g.* Gualda and Ghiorso, 2007; Hurwitz and Navon, 1994). There is no preferential spatial distribution of silicates or oxides within the samples, *i.e.* there are oxides, of different sizes, present in both the parts of the sample closer to the hotspot ("hotter") and in those further away from it ("colder" part). In many places, we can observe a silicate and an oxide crystal in close proximity, sometimes even an oxide between two silicate crystals, with bubbles nucleating first on the silicates, in every experiment (Figs. 7 and 8, sample 3-6).

A 2D axial slice from the *in situ* imaging that best shows bubble growth with time was selected (Fig. 7) and subsequently stacked into a time-lapse animation to illustrate the dynamic changes in the three-phase system during the experiments (electronic supplements 1 and 2), along with time-lapse animations of bubbles growing on the two different clinopyroxene crystal types in 3D (electronic supplements 3 and 4). A complete 3D visualization of the *ex situ* scans of samples 2b-8 and 3-6 from TOMCAT can be found in electronic supplement 5 and 6.

The *in situ* imaging allowed observation of the change in the contact angle during bubble growth, which is a dynamic property not obtainable in static scans. In cases where bubbles did not encounter neighbouring bubbles on the crystal surface, the contact angle between the bubbles and the clinopyroxene changes from a maximum of ~140° ± 5° to a minimum of ~50° ± 5° (measured on 15 bubbles through ~20 timesteps). When two bubbles come into contact their contact angles stop at 90°. In the latter case, bubbles do not coalesce; instead, they continue to grow outward into the melt. A thin layer of melt remains between the bubbles, and they do not detach from the clinopyroxene during the duration of the experiment (Fig. 6).

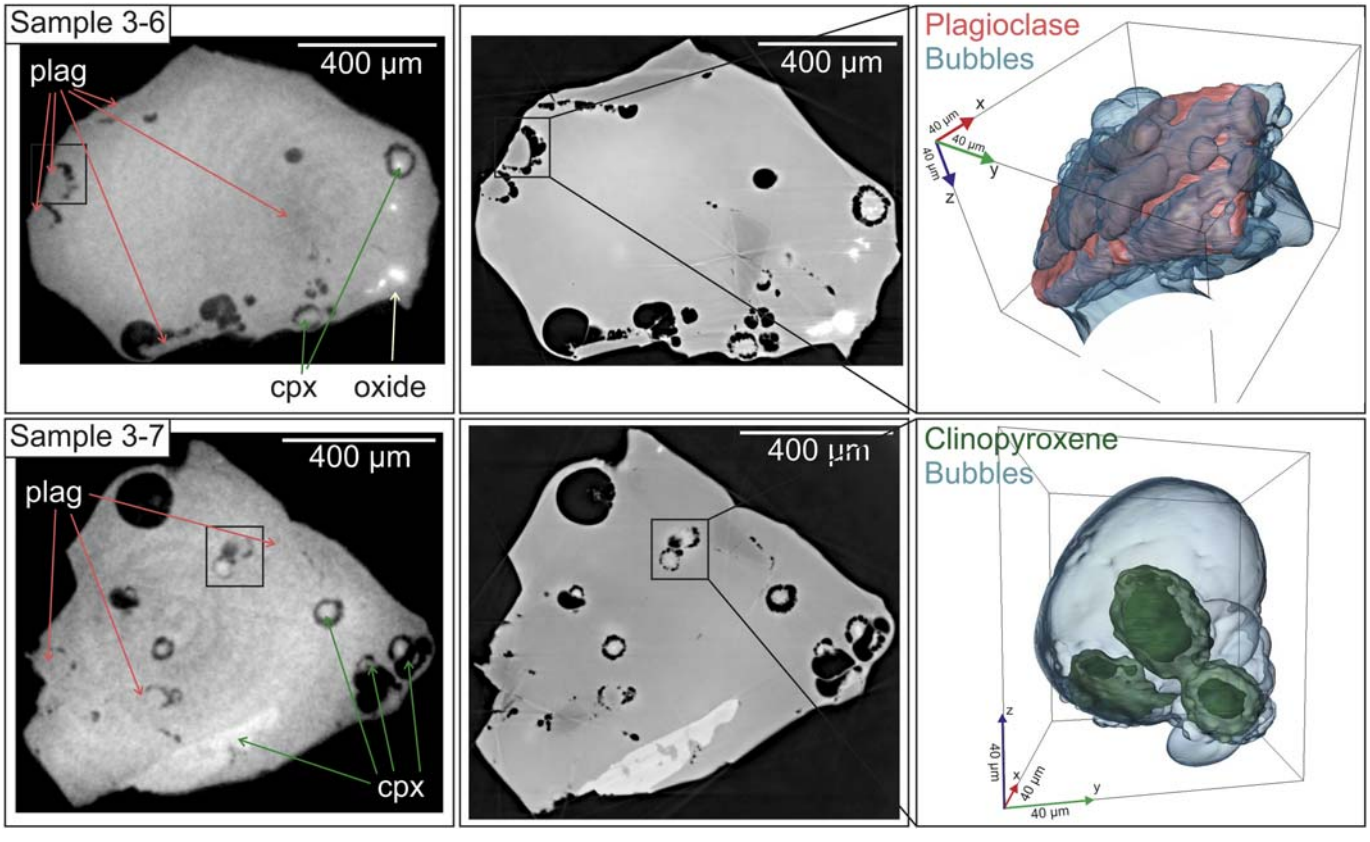

Fig. 8. A comparison between the *in situ* and the *ex situ* tomographic microscopy images. For both samples, the same slice is presented for both methods, followed by a 3D visualization of a clinopyroxene or a plagioclase crystal with their associated bubbles. The *in situ* slice corresponds to timestep t_{100}, and it's *ex situ* counterpart is not completely identical due to a time difference between the end of scanning and quenching. In the *ex situ* image of sample 3-6 we can see oxides within the melt, that grew during synthesis at high pressure, and have no bubbles on their surfaces. The lowermost bubble in the sample 3-6 plagioclase 3D visualization is faded out because a bubble from another crystal indented it. For sample 3-6 the slice presented here is located 525 µm above the slice presented in Fig. 7.

Bubbles on plagioclase crystals appear as continuous bubble films on the crystal surface and only with close inspection of the *ex situ* scans do the thin melt films between bubbles become visible (Fig. 7, sample 3-6). This suggests that bubbles nucleated individually on plagioclase surfaces, spread very quickly to occupy the available surface, all occurring below the 3 μm pixel size used in these experiments. In the bubbles that remained solitary on plagioclase crystals, the contact angle changes roughly from 120° ± 5° to 75° ± 5° (measured on 15 bubbles through ~20 timesteps).

Bubbles nucleated on oxide surfaces in the very last few timesteps (if at all; Fig. 6) and had a volume of only several voxels, which prevented the quantification of their contact angle change.

4. Discussion

We consider that the simplest explanation of our data is that bubbles nucleate directly on plagioclase and clinopyroxene in an andesitic magma. However, this finding is at odds with many earlier observations; hence we must verify that no other nucleation processes were active in our experiments. First, we discuss the possibility of bubble nucleation on cracks in the glassy sample or crypto-heterogeneities in the melt. Next, we consider the possible role of oxides as bubble nucleation sites in our experiments, and we show that the 2D images used in earlier studies can create the false idea that bubbles nucleate near crystals, rather than on crystal-melt interfaces. If bubbles can nucleate readily on plagioclase and clinopyroxene then there are other aspects of the process that may be important. Asperities and edges play a role in the nucleation of bubbles in some situations, but what was their role here? Finally, we discuss dynamic changes in the contact angle and the role of bubble detachment in magma degassing.

4.1. Lack of bubble nucleation on the cracks within the glass and crystals

We must discuss the possibility that bubble nucleation occurred on cracks in the charge (observed with a nanoCT) while the material was still a glass. If such cracks were nucleation sites then we would expect to see bubbles forming during *in situ* scanning in linear and planar arrays throughout the sample. This was never observed in these experiments; hence we conclude that bubbles have not nucleated on such cracks.

We must also consider the possibility that bubbles could have nucleated on small cracks that formed along the crystal-melt (or glass) boundaries due to the unequal expansion of crystals and glass during *in situ* heating. Coefficients of thermal expansion ($\alpha_{298\ K}$) are not well known for natural materials and the closest we could find are: $5.8 \times 10^{-6}\ °C^{-1}$ for anorthite glass (Arndt and Häberle, 1973) or $4.5 \times 10^{-6}\ °C^{-1}$ for aluminosilicate glass (Varshneya, 1994), $1.5 \times 10^{-5}\ °C^{-1}$ for plagioclase (five value average for $An_{78}Ab_{22}$ from Tribaudino et al., 2010), $3.33 \times 10^{-5}\ °C^{-1}$ for clinopyroxene (diopside, Cameron et al., 1973) and $2.06 \times 10^{-5}\ °C^{-1}$ for oxides (magnetite, Skinner, 1966). Based on these values, all the materials expand very similarly, but the smallest difference is between the plagioclase and the glass. Hence, if expansion cracks were the main reason for bubble nucleation, we would expect to see more bubbles nucleating on oxides and/or bubbles nucleating sooner on clinopyroxene than on plagioclase. We did not observe either phenomena and hence reject this hypothesis.

Additionally, the argument that nucleation occurs at expansion cracks implies that when bubbles start nucleating, the material around the crystal is a glass, and not a melt, in which case bubble nucleation and growth would cause further cracking of the glass, which again is never observed in these experiments. From the initial stages of nucleation and throughout their growth all bubbles display hemispherical topologies, indicating that they do not encounter any differential resistance from the surrounding material, which must be a melt. Two additional arguments in favour of melt, rather than glass, surrounding the crystals during bubble nucleation and growth are: 1) the temperatures at which the very first bubble nucleation events occurred (from 550 °C to 660 °C) are above the glass transition temperature for similar composition andesitic glasses (Giordano et al., 2005), 2) as heating commences and before bubble nucleation starts, we observe the annealing of quench cracks within the glass. However, where these cracks cut across a crystal, they do not anneal and the crystal expands (Fig. 7, sample 2b-8). No bubbles formed in the intra-crystalline cracks during these experiments, since the bubbles that formed on the outer crystal surfaces prevented the melt from entering this newly available space. It is easy to distinguish between these textures (un-annealed crystal cracks and the bubbles) because of their different orientation: the former cut through the crystal whereas the latter form along its boundaries. Furthermore, there is a time difference between their formations. When bubbles start to nucleate heterogeneously on silicate crystals that have an un-annealed crack, we do not observe the expansion of this crack along the crystal surface. Based on these arguments we conclude that the bubbles nucleated and grew within a melt and not a glass, and that cracks are not important for bubble nucleation in our experiments.

4.2. Lack of nucleation on crypto-heterogeneities in the melt

It has been proposed (Gardner et al., 1999) that nucleation could occur on solid structures within the melt smaller than can be detected with the image resolution used in this study. If this were the case in our experiments, then we would expect to observe two phenomena: First, these crypto-heterogeneities should be randomly present throughout the melt. Crystal melting did not occur or was minimal during the starting material synthesis, and the glass composition is the same both close to and far away from crystals. The SEM compositional analysis (electronic supplement 7) showed no difference in glass composition close to and further away from the crystal. Hence, we see no reason for localisation of crypto-heterogeneities closer to the crystals rather than further away from them. Second, if bubbles nucleated on crypto-heterogeneities close to the crystal instead on the crystal surface, we would see their shape change from spherical to hemispherical once they encounter the crystal surface. One could argue that in the first timesteps, where bubbles are identified by only a few voxels, there is not enough information to determine their shape. However, we would then also expect to see bubbles forming on such crypto-heterogeneities sufficiently far away from the crystal for us to be able to track their shape, yet, no bubbles are forming away from the crystal at the same time as those that form at the crystal-melt interface. Hence, we see no reason neither for localisation of crypto-heterogeneities closer to the crystals rather than further away from them nor for bubble nucleation on them. In the volumes imaged *ex situ*, bubble walls were inspected for the presence of small oxides or any other phases that could act as such heterogeneities, unobservable from *in situ* scans alone, and none were found.

4.3. Lack of nucleation adjacent to the crystals ("melt films")

Some recent studies have described the presence of bubbles close to silicate crystal surfaces, but separated from them by a melt film (*e.g.* Giachetti et al., 2010, 2011). However, we believe that this observation could be an artefact of observation in 2D. We show a similar situation in Fig. 9a–c, where a bubble was imaged by SEM in a section cut from sample 3-7, already imaged in 3D. If the SEM images were the only information at our disposal, we might have concluded that the bubble in question nucleated homogeneously in the melt, close to the crystal surface. However, in the reconstructed 3D volume it becomes clear that the 2D cross-section in question does not contain the bubble's maximum diameter. The maximum diameter plane is in fact located a few micrometers below the SEM cross-section, and there the bubble and plagioclase crystal are in contact. For the sample in question, the SEM cross-section contains other plagioclase crystals with bubbles in

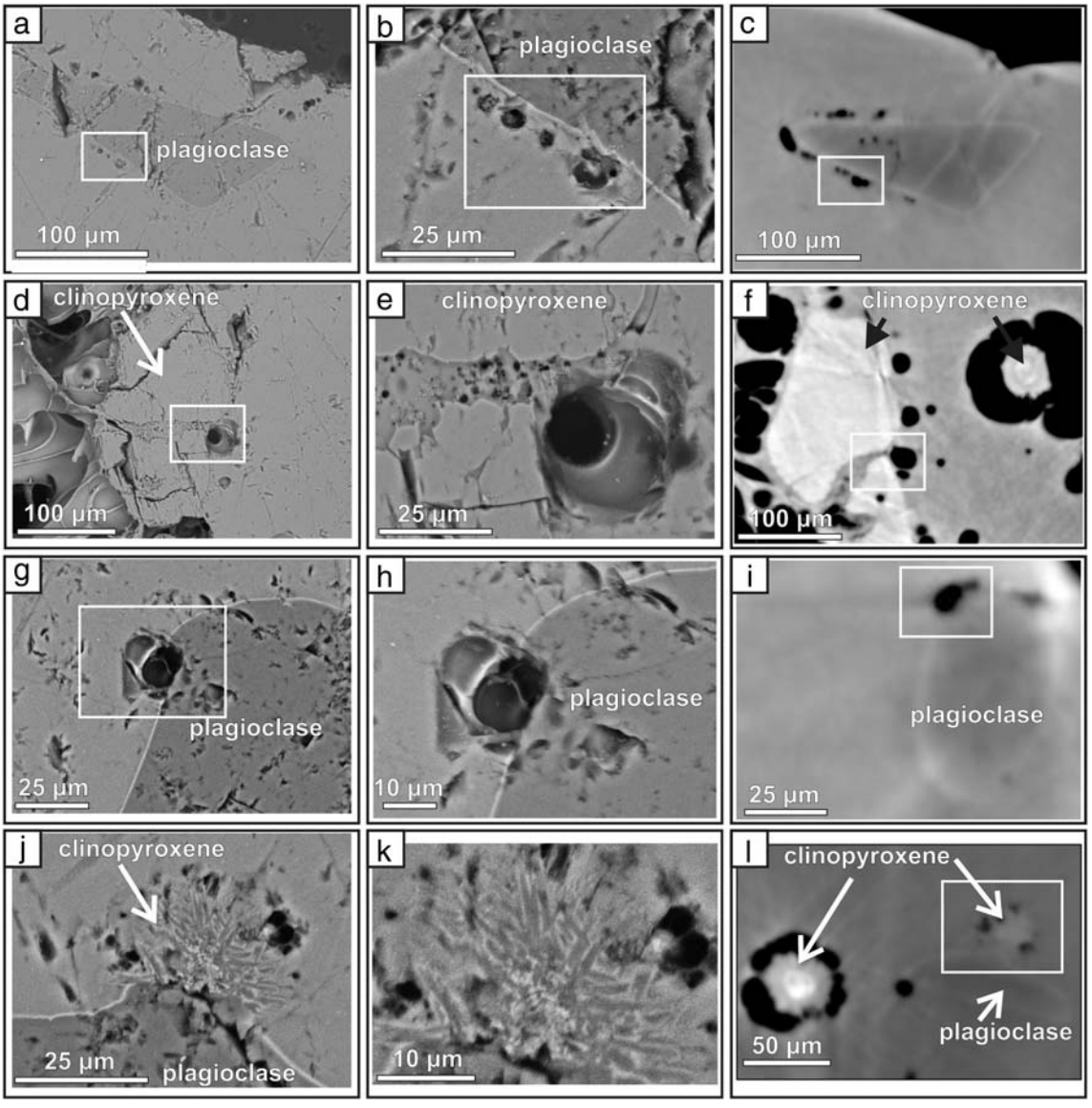

Fig. 9. Post-process images of sample 3-7, observed with a SEM and with propagation-based phase contrast synchrotron radiation microCT. Each of the 4 rows presents the same feature. There is an angular difference of 15° between the two methods, so the scans are not identical. a, b) Plagioclase crystal imaged with SEM. A series of bubbles can be seen very close to the plagioclase border. Only the one of the furthest right side appears to be in contact with the jagged surface of the plagioclase. c) The same plagioclase crystal, seen with propagation-based imaging. The pale line along the border of the crystal is the x-ray equivalent to the Becke line. Due to the tilt between the two different planes, image c is 10 μm below images a and b, but on it we see all the bubbles in direct contact with the plagioclases – an example that demonstrates how 2D observations can lead to erroneous assumptions. d, e) Clinopyroxene crystal with bubbles on its surfaces. We see the bubble in direct contact and a part of the crystal that presumably started melting. f) The same clinopyroxene crystal seen from a slightly tilted plane. We see more bubbles on the right-hand side, with a hemispherical topology, due to contact with the crystal. g, h) Plagioclase crystal with a bubble on its surface. The zoomed image shows the absence of any melt film between the bubble and the plagioclase. i) The same bubble on the tilted plane. We see the contact area between the bubble and the plagioclase is now larger and that the curvature of the bubble follows the surface of the plagioclase. j, k) A plagioclase and a clinopyroxene crystal in contact. Only the outer rim of the clinopyroxene is visible, with bubbles around it. We see the outer rim consists of spikes (compositionally the same to the core) and that bubbles are located in between the spikes. l. On the lower magnification propagation-based image we can observe two clinopyroxenes and we see that the one on the left-hand side has larger bubbles on its outer rim, which appear unaffected by its spiked surface.

contact with their surfaces (Fig. 9g–i), but this example shows the importance of 3D (and 4D) imaging in correctly identifying a bubble's position.

For comparative purposes, we imaged two natural samples, one andesitic from Montserrat and the other basaltic from Stromboli (Fig. 10). The textures produced around silicate crystals present in both those samples are very similar to those in our *in situ* scans, and can also be compared to other published textures (*e.g.* Giachetti et al., 2010, 2011; Hurwitz and Navon, 1994). All examples lack a melt film between the plagioclase crystals and the bubbles, based on microCT *ex situ* scans. Due to our *in situ* observations, the mechanisms that produce such textures can now be explained as bubbles nucleating on the silicate-melt interfaces and growing outward instead of the previous explanation of bubbles nucleating elsewhere in the melt and growing towards the silicate crystals (*e.g.* Giachetti et al., 2010).

4.4. Bubble nucleation and surface asperities

In many studies in volcanology, material science and fluid dynamics, the surface characteristics of a potential bubble nucleation site are regarded as extremely important (*e.g.* Atchley and Prosperetti, 1989; Hurwitz and Navon, 1994). It is generally accepted that the rougher parts of an interface are less wetted by the surrounding liquid/melt, and hence have a higher potential for heterogeneous bubble nucleation (Atchley and Prosperetti, 1989; Blander and Katz, 1975; Cole, 1974). At the 3 μm resolution of the *in situ* tomography, the surfaces of

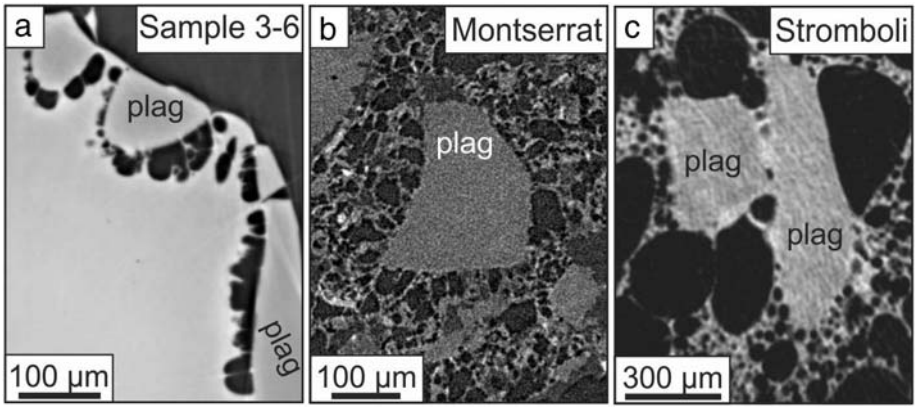

Fig. 10. Comparison of bubble-crystal textures in experimental charges and natural samples visualized using microtomography. Plag = plagioclase. a. Experimental sample 3-6 of andesitic composition. Three plagioclase crystals are visible on the outer border of the melt, each surrounded by bubbles that nucleated and grew on the crystal surface. b. Natural sample from Monserrat, of andesitic composition. In the center of the image, there is a plagioclase crystal in contact with gas bubbles. The longer axis of the majority of the bubbles appears perpendicular to the plagioclase surface, giving the appearance of an arrangement of bubbles radiating from the crystal outward. c. Natural sample from Stromboli, of basaltic composition, with another plagioclase crystal in contact with bubbles. We see both large and small bubbles, all following the crystal's surface morphology. Cases such as b and c were until know interpreted as bubbles growing towards a crystal (*e.g.* Giachetti et al., 2010), after nucleating elsewhere.

clinopyroxene appear smooth and the plagioclase surface is not visible; hence we examined both minerals at higher resolution with phase contrast *ex situ* tomography and scanning electron microscopy (Fig. 8). The plagioclase crystals have very angular morphologies, consistent with fracture along cleavage planes and show no signs of melting during starting material synthesis. *Ex situ* phase contrast revealed that bubbles are on plagioclase surfaces but give no additional information on the surfaces themselves, as they appear smooth at a resolution of 0.65 µm. Scanning electron microscopy did reveal the presence of some crevices with bubbles (Fig. 9a–c). In *ex situ* phase contrast, both the clinopyroxene core and rim surfaces appear smooth, however scanning electron microscopy revealed that the outer rim surface is in fact highly irregular and full of pits (Fig. 9j–l) visible at a resolution of 0.65 µm. However, for both plagioclase and clinopyroxene, bubbles have nucleated on both the irregular and the smooth parts of the crystals. Hence, the irregularities present acted as nucleation sites, but there is no evidence to suggest that nucleation occurred more frequently at asperities than at what appear to be smooth surfaces at the maximum resolution used in this study.

4.5. Effect of crystal edges on bubble nucleation and growth

Conventional heterogeneous bubble nucleation theory (Navon and Lyakhovsky, 1998) shows that changes in the surface energies involved in a crystal-bubble-melt assemblage (equations found in Hurwitz and Navon, 1994), would be manifested by a change in the bubble-crystal contact angle. The crystals' contribution to the crystal-melt and the crystal-bubble surface energy would then be dependent on the crystal plane in question, as different crystallographic planes have different surface energies (Eustathopoulos et al., 1999). Furthermore, if a bubble, while spreading on a crystal surface were to encounter a change in the crystal plane, such as a crystal edge or corner, the abrupt surface energy change would make it an ideal place for bubble growth to stop or perhaps to induce a rapid change in contact angle that could cause the bubble to detach. The plagioclase crystals and large clinopyroxene crystals in our study exhibit such angular morphologies, where cleavage planes intersect (Fig. 7, sample 2b-8). During the *in situ* scanning, we observed bubbles forming on cleavage plane surfaces and spreading along them. When they encountered a crystal edge, bubbles extended around it and continued to spread on the new crystallographic plane with no change or pause in growth rate. This observation leads us to conclude that either the surface energy differences between crystallographic planes of a single crystal are not different enough to affect the assemblages' combined surface energy, or that perhaps the assemblage is not so sensitive to surface energy changes. This is also visible for clinopyroxenes with spiked outer rims, where bubbles on the spiked rim have grown to sizes much larger than a single spike, *i.e.* they are in contact with several spikes, but do not seem to be influenced by such an irregular surface (Fig. 9k, l). The possibility of the crystal-melt surface energy not playing as big of a role in the melt-crystal-bubble assemblage as previously thought might be why silicate crystals were favoured over oxides as bubble nucleation sites in our experiments.

4.6. Contact angle changes and possible bubble detachment

The bubble contact angle is an extremely important parameter, yet much of the existing data have significant limitations. Firstly, in all studies thus far (Fig. 2), the measurement of the contact angle was done in 2D and the value assumed to be representative of the actual, 3D value. This may not be correct and such data must be viewed with caution. Secondly, contact angles are frequently observed in the final, static state of the sample. It is evident that contact angles change as bubbles grow and this can only be recognized in dynamic observations. In our study the bubble contact angle on both plagioclase and clinopyroxene surfaces decreased with time, at least until a neighbouring bubble was encountered. A decreasing trend in the contact angle leads us to consider that there is a possibility that it would continue to decrease to zero, if a bubble was solitary, at which point the bubble will detach from the crystal (a zero degree contact angle implies no contact).

Gualda and Ghiorso (2007) considered that a bubble-silicate crystal pair would tend to detach, contrary to a bubble-oxide pair that would tend to remain attached. Our decreasing contact angles is in agreement with their findings, since it is intuitively clear that detachment of any bubble from any surface would be expressed by an angle decrease, while attachment would be expressed through a contact angle increase. This process (contact angle hysteresis) is well documented and extensively studied in chemistry, material sciences and engineering (*e.g.* Hirth et al., 1970; Whyman et al., 2008).

Even though we observed a consistent decrease in the contact angle, we did not observe bubble detachment during our experiments. This was anticipated due to the low water content in our samples (0.25–0.5 wt% H_2O) and the short experimental duration (50 s). If we were to take for example an andesite with 6 wt% H_2O and a viscosity of 10 Pa s, and using Stokes' law velocity, it would take a bubble of 100 µm radius 3.3 s to move 10 µm away from its initial location. In our case, the water content is much lower, hence the viscosity is higher and the bubble velocity is orders of magnitude slower. Since the imaging of bubble development was the primary aim of our experiments, we stopped scanning

before any potential detachment could take place. In our experiments, complete detachment would also be difficult to observe due to homogeneous bubble nucleation that takes place as the temperature rises and essentially fills up all the space within the sample. Additionally, our heterogeneously nucleated bubbles are not solitary, but in contact one with the other and thus they interact with one another. This makes it harder for a solitary bubble to detach from the bubble cluster formed on the crystal surface. In a natural system, solitary bubble detachment from a crystal surface would occur when the critical radius of either bubble or crystal is surpassed (*i.e.* when the detachment force becomes greater than the attachment force; Gualda and Ghiorso, 2007), if at that point, there is space available in the surrounding melt (*i.e.* homogeneous bubble nucleation has not yet occurred).

We envision two possible mechanisms of bubble cluster detachment: simple cluster detachment and coalescence induced detachment (Fig. 11). 1) If the bubble cluster does not encompass the crystal's entire surface, at a certain point along the bubble-crystal-melt contact line, melt can protrude between the flank bubble(s) and the crystal, at the point in time when the detachment force surpasses the attachment one (forces defined in Gualda and Ghiorso, 2007). This could lead to a chain reaction, where after the first bubble starts to detach, it's immediate neighbours follow suite, preferring to maintain the bubble cluster intact than to remain on the silicate crystal surface. 2) Instead of maintaining individual thin melt films between each neighbouring bubble, in an effort to reduce the bubble cluster's total surface energy, bubble coalescence occurs (either between just two neighbouring bubbles, or more). This coalescence event leads to an abrupt bubble-crystal contact angle change and the total surface energy decreases, provoking bubble detachment. Both hypotheses would be possible if heterogeneous bubble nucleation is the primary nucleation process, and homogeneous nucleation is secondary. In both hypotheses the silicate crystal surface is reactivated for the nucleation of new bubbles. It is this possibility that makes silicate crystals much more interesting than oxide crystals for the study of bubble nucleation and magma degassing.

5. Conclusions

Our findings show that heterogeneous bubble nucleation on silicates can occur in magma and should not be ignored. We also demonstrate a decreasing trend in bubble-crystal contact angles, indicating a tendency for detachment, in accordance with published work on low silicate crystal-bubble affinity (Gualda and Ghiorso, 2007). This indicates that silicate crystals can generate bubbles and subsequently lose them, thereby freeing their surfaces to nucleate bubbles again.

Combining heterogeneous bubble nucleation on silicate crystals with the possibility of detachment could offer an explanation as to why in many natural and experimental systems there are more bubbles found than oxide crystals could be expected to produce (see Shea, 2017). Instead of homogeneously nucleating within the melt, as generally proposed, the excess of bubbles could have been generated on silicate crystal surfaces present in these systems. We show that heterogeneous bubble nucleation on silicates is possible, and that, given the possibilities of 4D imaging and in the light of our findings, the explanations for certain textures in both natural and experimental samples should be reconsidered. We emphasize that observing the contact angle change (increase or decrease) *via* time-resolved, *in situ* experiments is the best way of determining a bubble's affinity for a crystal surface. We were also able to directly confirm that the contact angle changes during bubble growth and that the post-process angles reported thus far in the literature are unlikely to be true angles, as suggested by Gardner and Denis (2004).

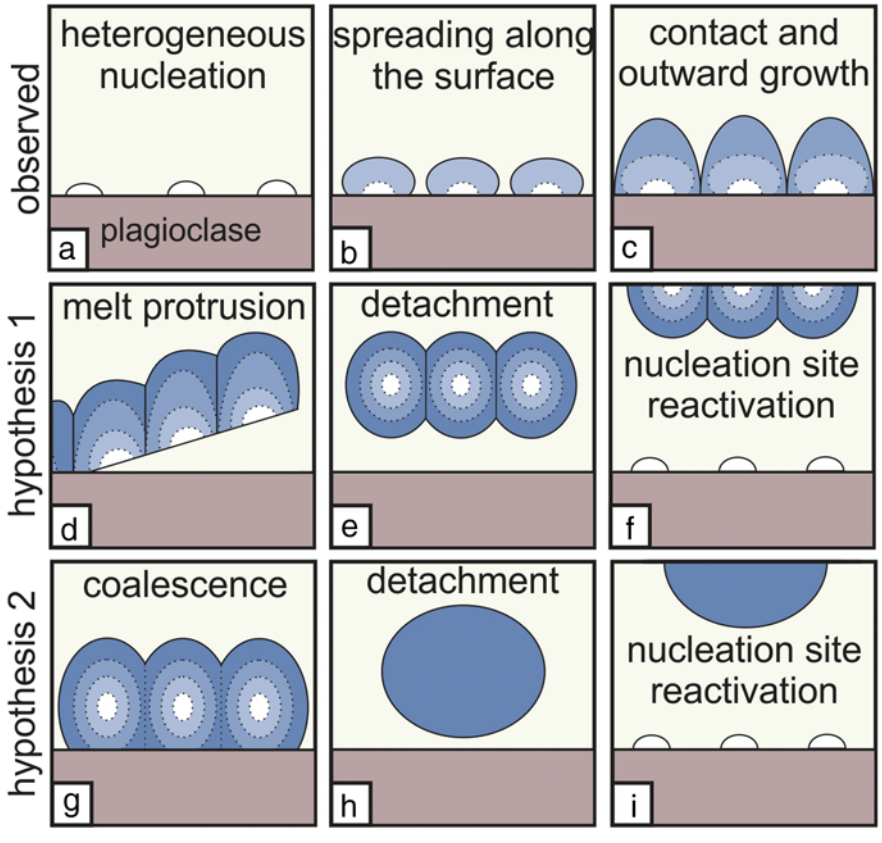

Fig. 11. Possible bubble-crystal detachment scenarios. a–c) Schematic representation of observed bubble growth during *in situ* experiments. d–f) Hypothesis 1 for bubble detachment from a silicate crystal surface. Here, the flank bubbles start to detach first and the rest follow, preserving a bubble cluster. g–i) Hypothesis 2 for bubble detachment from a silicate crystal surface. Here, bubble coalescence occurs first, and the decrease in bubble surface energy provokes detachment.

The minimum number of bubbles that nucleated on minerals in our experiments can be used to demonstrate the relative bubble nucleation efficiencies of their surfaces. Such a comparison can be safely made within our experimental suite, wherein every sample the melt composition, individual mineral species composition and initial water concentration were constant. In other words, the only changing parameters between different minerals were the crystal-melt and crystal-bubble surface energy, so we can say that the silicate crystals were more efficient than the oxides. It is very tempting to apply this difference in efficiency to other systems with different melt and mineral compositions and water concentrations; however, the authors warn against making direct extensions without further experiments. Nevertheless, our finding that clinopyroxene and plagioclase crystals dominate as sites of bubble nucleation in andesitic melts shows that the possible effect of these crystals on vesiculation and therefore the effusive to explosive transition (Bai et al., 2011) should be taken into account.

If the role of silicate crystals in bubble nucleation is viewed in this light, their importance in bubble nucleation models and eruption prediction models changes considerably, from being an almost neglected parameter to becoming perhaps one of the governing ones – a phenomenon worthy of further research.

Supplementary data to this article can be found online at https://doi.org/10.1016/j.lithos.2017.11.024.

Acknowledgements

We acknowledge the staff at the TOMCAT beamline for their support during the experiments. A portion of this work was performed at GeoSoilEnviroCARS (The University of Chicago, Sector 13), Advanced Photon Source (APS), Argonne National Laboratory. GeoSoilEnviroCARS is supported by the National Science Foundation - Earth Sciences (EAR-1128799) and Department of Energy - GeoSciences (DE-FG02-94ER14466). This research used resources of the Advanced Photon Source, a U.S. Department of Energy (DOE) Office of Science User Facility operated for the DOE Office of Science by Argonne National Laboratory under Contract No. DE-AC02-06CH11357. All authors wish to thank Mark Rivers (APS) for help with acquiring the *ex situ* scan of the natural sample from Montserrat. P.P. wishes to thank Marko Kudrna Prašek for many useful discussions, and all authors wish to thank Fabio Arzilli and Matteo Masotta for their insightful and helpful reviews.

Funding

This work was supported by NSERC (Canada) Discovery grants to M.D.H. (RGPIN 2012-25137) and D.R.B. (grant number RGPIN-2015-06355). The travel costs for the work carried at the APS were supported by the Mineralogical Association of Canada Student Travel/Research Grant 2014 awarded to P.P. The authors acknowledge the EXTREMA COST Action MP 1207 for networking support.

Author contributions

P.P. (PhD student and principal investigator), D.R.B. (PhD co-director), J.C. (undergraduate student), J.L.F. (beamline scientist at the TOMCAT beamline), L.M., G.L. and F.B. all performed the tomographic microscopy experiments. P.P., M.D.H. (PhD director) and D.R.B. contributed to the ideas developed in the paper. J.C. synthesized the starting materials, J.L.F., L.M. and F.B. performed the fine-tuning of the acquisition and reconstruction parameters at TOMCAT. P.P. performed the volume rendering, manual thresholding, isosurface generation and contact angle measurements. All authors assisted with the manuscript.

Additional information

Supplementary information is available in the online version of the paper. All correspondence and material requests should be directed to P.P.

Competing financial interests

None.

References

Acocella, V., 2014. Structural control on magmatism along divergent and convergent plate boundaries: overview, model, problems. Earth-Science Reviews 136, 226–288.

Adamson, A.W., Gast, A., 1997. Physical Chemistry of Surfaces. sixth ed. John Wiley and Sons, New York.

Applegarth, L.J., Tuffen, H., James, M.R., Pinkerton, H., Cashman, K.V., 2013. Direct observations of degassing-induced crystallization in basalts. Geology 41 (2), 243–246.

Arndt, J., Häberle, F., 1973. Thermal expansion and glass transition temperatures of synthetic glasses of plagioclase-like compositions. Contributions to Mineralogy and Petrology 39 (2), 175–183.

Atchley, A.A., Prosperetti, A., 1989. The crevice model of bubble nucleation. The Journal of the Acoustical Society of America 86 (3), 1065–1084.

Bagdassarov, N.S., Dingwell, D.B., Wilding, M.C., 1996. Rhyolite magma degassing: an experimental study of melt vesiculation. Bulletin of Volcanology 57 (8), 587–601.

Bai, L., Baker, D.R., Rivers, M., 2008. Experimental study of bubble growth in Stromboli basalt melts at 1 atm. Earth and Planetary Science Letters 267 (3), 533–547.

Bai, L., Baker, D.R., Polacci, M., Hill, R.J., 2011. In-situ degassing study on crystal-bearing Stromboli basaltic magmas: implications for Stromboli explosions. Geophysical Research Letters 38 (17), L17309.

Baker, D.R., Eggler, D.H., 1987. Compositions of anhydrous and hydrous melts coexisting with plagioclase, augite, and olivine or low-Ca pyroxene from 1 atm to 8 kbar; application to the Aleutian volcanic center of Atka. American Mineralogist 72 (1–2), 12–28.

Baker, D.R., Brun, F., O'Shaughnessy, C., Mancini, L., Fife, J.L., Rivers, M., 2012a. A four-dimensional X-ray tomographic microscopy study of bubble growth in basaltic foam. Nature Communications 3, 1135.

Baker, D.R., Mancini, L., Polacci, M., Higgins, M.D., Gualda, G.A.R., Hill, R.J., Rivers, M.L., 2012b. An introduction to the application of X-ray microtomography to the three-dimensional study of igneous rocks. Lithos 148, 262–276.

Belien, I.B., Cashman, K.V., Rempel, A.W., 2010. Gas accumulation in particle-rich suspensions and implications for bubble populations in crystal-rich magma. Earth and Planetary Science Letters 297 (1–2), 133–140.

Blander, M., Katz, J.L., 1975. Bubble nucleation in liquids. AICHE Journal 21 (5), 833–848.

Blythe, L.S., Deegan, F.M., Freda, C., Jolis, E.M., Masotta, M., Misiti, V., Taddeucci, J., Troll, V.R., 2015. CO_2 bubble generation and migration during magma–carbonate interaction. Contributions to Mineralogy and Petrology 169 (4), 1–16.

Brun, F., Mancini, L., Kasae, P., Favretto, S., Dreossi, D., Tromba, G., 2010. Pore3D: a software library for quantitative analysis of porous media. Nuclear Instruments and Methods in Physics Research Section A: Accelerators, Spectrometers, Detectors and Associated Equipment 615 (3), 326–332.

Cameron, M., Sueno, S., Prewitt, C.T., Papike, J.J., 1973. High-temperature crystal chemistry of acmite, diopside, hedenbergite, jadeite, spodumene, and ureyite. American Mineralogist 58, 594–618.

Cluzel, N., Laporte, D., Provost, A., Kannewischer, I., 2008. Kinetics of heterogeneous bubble nucleation in rhyolitic melts: implications for the number density of bubbles in volcanic conduits and for pumice textures. Contributions to Mineralogy and Petrology 156 (6), 745–763.

Cole, R., 1974. Boiling nucleation. Advances in Heat Transfer 10, 85–166.

Eichelberger, J., Hayes, D., 1982. Magmatic model for the Mount St. Helens blast of May 18, 1980. Journal of Geophysical Research 87 (B9), 7727–7738.

Eustathopoulos, N., Nicholas, M.G., Drevet, B., 1999. Wettability at High Temperatures. Vol. 3. Elsevier, Amsterdam.

Fiege, A., Cichy, S.B., 2015. Experimental constraints on bubble formation and growth during magma ascent: a review. American Mineralogist 100 (11—12), 2426–2442.

Fife, J.L., Rappaz, M., Pistone, M., Celcer, T., Mikuljan, G., Stampanoni, M., 2012. Development of a laser-based heating system for in situ synchrotron-based X-ray tomographic microscopy. Journal of Synchrotron Radiation 19 (3), 352–358.

Gardner, J.E., 2007. Heterogeneous bubble nucleation in highly viscous silicate melts during instantaneous decompression from high pressure. Chemical Geology 236 (1–2), 1–12.

Gardner, J.E., Denis, M.-H., 2004. Heterogeneous bubble nucleation on Fe–Ti oxide crystals in high-silica rhyolitic melts. Geochimica et Cosmochimica Acta 68 (17), 3587–3597.

Gardner, J.E., Thomas, R.M.E., Jaupart, C., Tait, S., 1996. Fragmentation of magma during Plinian volcanic eruptions. Bulletin of Volcanology 58 (2–3), 144–162.

Gardner, J.E., Hilton, M., Carroll, M.R., 1999. Experimental constraints on degassing of magma: isothermal bubble growth during continuous decompression from high pressure. Earth and Planetary Science Letters 168 (1), 201–218.

Gardner, J.E., Hilton, M., Carroll, M.R., 2000. Bubble growth in highly viscous silicate melts during continuous decompression from high pressure. Geochimica et Cosmochimica Acta 64 (8), 1473–1483.

Giachetti, T., Druitt, T.H., Burgisser, A., Arbaret, L., Galven, C., 2010. Bubble nucleation, growth and coalescence during the 1997 Vulcanian explosions of Soufrière Hills Volcano, Montserrat. Journal of Volcanology and Geothermal Research 193 (3), 215–231.

Giachetti, T., Burgisser, A., Arbaret, L., Druitt, T.H., Kelfoun, K., 2011. Quantitative textural analysis of Vulcanian pyroclasts (Montserrat) using multi-scale X-ray computed microtomography: comparison with results from 2D image analysis. Bulletin of Volcanology 73 (9), 1295–1309.

Giordano, D., Nichols, A.R.L., Dingwell, D.B., 2005. Glass transition temperatures of natural hydrous melts: a relationship with shear viscosity and implications for the welding process. Journal of Volcanology and Geothermal Research 142 (1), 105–118.

Gondé, C., Massare, D., Bureau, H., Martel, C., Pichavant, M., Clocchiatti, R., 2006. In situ study of magmatic processes: a new experimental approach. High Pressure Research 26 (3), 243–250.
Gondé, C., Martel, C., Pichavant, M., Bureau, H., 2011. In situ bubble vesiculation in silicic magmas. American Mineralogist 96 (1), 111–124.
Gualda, G.A., Anderson, 2007. Magnetite scavenging and the buoyancy of bubbles in magmas. Part 1: discovery of a pre-eruptive bubble in Bishop rhyolite. Contributions to Mineralogy and Petrology 153 (6), 733–742.
Gualda, G.A., Ghiorso, M.S., 2007. Magnetite scavenging and the buoyancy of bubbles in magmas. Part 2: energetics of crystal-bubble attachment in magmas. Contributions to Mineralogy and Petrology 154 (4), 479–490.
Hirth, J., Pound, G.M., Pierre, G.R.St., 1970. Bubble nucleation. Metallurgical Transactions 1 (4), 939–945.
Hurwitz, S., Navon, O., 1994. Bubble nucleation in rhyolitic melts: experiments at high pressure, temperature, and water content. Earth and Planetary Science Letters 122 (3–4), 267–280.
Landau, L., Lifshitz, E., 1980. Statistical Physics, Vol. 1. 24. Pergamon, Oxford, pp. 31–57.
Larsen, J.F., 2008. Heterogeneous bubble nucleation and disequilibrium H_2O exsolution in Vesuvius K-phonolite melts. Journal of Volcanology and Geothermal Research 175 (3), 278–288.
Manga, M., Brodsky, E., 2006. Seismic triggering of eruptions in the far field: volcanoes and geysers. Annual Review of Earth and Planetary Sciences 34, 263–291.
Mangan, M., Sisson, T., 2000. Delayed, disequilibrium degassing in rhyolite magma: decompression experiments and implications for explosive volcanism. Earth and Planetary Science Letters 183 (3), 441–455.
Mangan, M., Sisson, T., 2005. Evolution of melt-vapor surface tension in silicic volcanic systems: experiments with hydrous melts. Journal of Geophysical Research - Solid Earth 110 (B1), B01202.
Mangan, M., Sisson, T.W., Hankins, W.B., 2004. Decompression experiments identify kinetic controls on explosive silicic eruptions. Geophysical Research Letters 31 (8), L08605.
Masotta, M., Ni, H., Keppler, H., 2014. In situ observations of bubble growth in basaltic, andesitic and rhyodacitic melts. Contributions to Mineralogy and Petrology 167 (2), 1–14.
Mokso, R., Schlepütz, C.M., Theidel, G., Billich, H., Schmid, E., Celcer, T., Mikuljan, G., Sala, L., Marone, F., Schlumpf, N., Stampanoni, M., 2017. GigaFRoST: the gigabit fast readout system for tomography. Journal of Synchrotron Radiation 24:1250–1259. https://doi.org/10.1107/S1600577517013522.
Mourtada-Bonnefoi, C.C., Laporte, D., 2004. Kinetics of bubble nucleation in a rhyolitic melt: an experimental study of the effect of ascent rate. Earth and Planetary Science Letters 218 (3), 521–537.
Mysen, B., Richet, P., 2005. Silicate Glasses and Melts: Properties and Structure. 10. Elsevier Science, p. 525.
Navon, O., Lyakhovsky, V., 1998. Vesiculation processes in silicic magmas. Geological Society, London, Special Publications 145 (1), 27–50.
Paganin, D., Mayo, S.C., Gureyev, T.E., Wilkins, P.R., Wilkins, S.W., 2002. Simultaneous phase and amplitude extraction from a single defocused image of a homogeneous object. Journal of Microscopy 206, 33–40.
Pistone, M., Arzilli, F., Dobson, K.J., Cordonnier, B., Reusser, E., Ulmer, P., Marone, F., Whittington, A.G., Mancini, L., Fife, J.L., Blundy, J.D., 2015a. Gas-driven filter pressing in magmas: insights into in-situ melt segregation from crystal mushes. Geology 43, 699–702.
Pistone, M., Caricchi, L., Fife, J.L., Mader, K., Ulmer, P., 2015b. In situ X-ray tomographic microscopy observations of vesiculation of bubble-free and bubble-bearing magmas. Bulletin of Volcanology 77 (12), 1–15.
Polacci, M., Baker, D.R., Mancini, L., Tromba, G., Zanini, F., 2006. Three-dimensional investigation of volcanic textures by X-ray microtomography and implications for conduit processes. Geophysical Research Letters 33 (13), L13312.
Proussevitch, A., Sahagian, D., 2005. Bubbledrive-1: a numerical model of volcanic eruption mechanisms driven by disequilibrium magma degassing. Journal of Volcanology and Geothermal Research 143 (1), 89–111.
Sakuyama, M., Kushiro, I., 1979. Vesiculation of hydrous andesitic melt and transport of alkalies by separated vapor phase. Contributions to Mineralogy and Petrology 71 (1), 61–66.
Schindelin, J., Arganda-Carreras, I., Frise, E., Kaynig, V., Longair, M., Pietzsch, T., Preibisch, S., Rueden, C., Saalfeld, S., Schmid, B., Tinevez, J.Y., 2012. Fiji: an open-source platform for biological-image analysis. Nature Methods 9 (7), 676–682.
Shea, T., 2017. Bubble nucleation in magmas: a dominantly heterogeneous process? Journal of Volcanology and Geothermal Research 343, 155–170.
Sigurdsson, H., Houghton, B., McNutt, S., Rymer, H., Stix, J. (Eds.), 2015. The Encyclopedia of Volcanoes. Elsevier, Amsterdam.
Skinner, B.J., 1966. Section 6: thermal expansion. Geological Society of America Memoirs 97, 75–96.
Sparks, R.S.J., 1978. The dynamics of bubble formation and growth in magmas: a review and analysis. Journal of Volcanology and Geothermal Research 3 (1–2), 1–37.
Stampanoni, M., Groso, A., Isenegger, A., Mikuljan, G., Chen, Q., Bertrand, A., Henein, S., Betemps, R., Frommherz, U., Böhler, P., Meister, D., Lange, M., Abela, R., 2006. Trends in synchrotron-based tomographic imaging: the SLS experience. Proceedings SPIE, 6318, Developments in X-Ray Tomography V, 63180M (September 07, 2006).
Tribaudino, M., Angel, R.J., Cámara, F., Nestola, F., Pasqual, D., Margiolaki, I., 2010. Thermal expansion of plagioclase feldspars. Contributions to Mineralogy and Petrology 160 (6), 899–908.
Varshneya, A.K., 1994. Fundamentals of Inorganic Glasses. first ed. Academic Press, Inc., San Diego.
Whyman, G., Bormashenko, E., Stein, T., 2008. The rigorous derivation of Young, Cassie–Baxter and Wenzel equations and the analysis of the contact angle hysteresis phenomenon. Chemical Physics Letters 450 (4), 355–359.
Young, T., 1805. An essay on the cohesion of fluids. Philosophical Transactions of the Royal Society of London 95, 65–87.